Experimental investigation and SOLPS-ITER modeling of Ne-seeded radiative divertor H-modes plasma on EAST

Jingbo Chen[1,2], Zhongshi Yang[1,*], David Coster[3], Kedong Li[1,2], Kai Wu[1,2], Yanmin Duan[1], Liang Wang[1], Jichan Xu[1,2], Xiahua Chen[1,2], Fang Ding[1], Qing Zang[1], Yumin Wang[1], Jinhua Wu[1], Guang-Nan Luo[1,2] and EAST Team[1]

1. Institute of Plasma Physics, Chinese Academy of Sciences, Hefei, 230031, China
2. University of Science and Technology of China, Hefei, 230000, China
3. Max-Planck-Institut für Plasmaphysik, Garching, 85748, Germany

Abstract:

Both experimental and numerical modeling were carried out on EAST to study the radiative divertor plasma behavior with neon (Ne) seeding. Steady H-mode radiation feedback control regimes (f_{rad}~18-36%) were achieved by synergistic working of a divertor puff and supersonic molecular beam injection (SMBI) with Ne in the 2017 EAST campaign. Ne seeding effectively promoted divertor detachment while only causing a slight loss to the plasma stored energy in the experiment. To better understand the experimental result, analysis of the detachment process is introduced in this work. Two time slices namely before and after Ne seeding during the radiative divertor experiment in Shot #71021 were simulated by SOLPS-ITER code. The simulation results for upstream plasma agreed well with the experiment, and the divertor profile agreed well on the outer targets when ignoring drifts. Radiation distribution was also calculated by SOLPS-ITER, showing that there was a high radiation region near the X-point, which is consistent with the experimental measurements.

1. Introduction

With the higher power in ITER and future devices, there will be a critical issue for power exhaust due to the limit of heat load capacity for divertor target materials. Seeding extrinsic impurities, such as nitrogen (N_2), argon (Ar) and neon (Ne), has been proved to be an effective method mitigating high particle flux and heat load on divertor targets in several tokamaks[1]. In ASDEX Upgrade, N_2 and Ar as the extrinsic radiators show their high efficiency in promoting divertor detachment in both experiment and simulation studies[2-5]. Other tokamaks, like DIII-D[6], JET[7], JT-60U[8] and Alcator C-mod[9] also carried out a series of investigations to study plasma behavior and the physics of divertor detachment with impurity seeding.

Experimental Advanced Superconductive Tokamak (EAST) aims at long pulse and high-performance plasmas in the future[10]. Although EAST has upgraded its upper divertor into ITER-like water cooling mono-block tungsten (W) divertor, meaning the ability of withstanding high heat flux has been improved significantly, the heat load issue is still a serious challenge with the increase of heating power[11, 12]. To effectively control the heat load on divertor targets and achieve steady long-pulse plasmas with high power injection, investigations including experiments and modeling with impurity seeding have been carried out in recent EAST campaigns[13, 14]. In current tokamaks, N_2 appears superior performance in divertor cooling and core confinement improvement[15]. However, owing to the routine Li-coating wall condition in EAST, N_2 cannot be a radiating candidate because N_2 easily reacts with hydrogen and lithium and forms toxic and explosive products, such as NH_3, and LiN_3. Therefore, Ar and Ne are the best choices under current conditions

*Corresponding author E-mail: zsyang@ipp.ac.cn

for EAST. Previous experimental results of Ar seeding showed that Ar is highly efficient at cooling down plasma into detachment, which is verified by SOLPS 5.0 simulations. However, reduced confinement due to Ar enrichment in the core region and W sputtering on the divertor targets was observed during Ar seeding along with a high radiation loss to the plasma. Compared with Ar, Ne has a considerable cooling efficiency but is also thought to be a Low-Z impurity to avoid plasma facing components (PFCs) sputtering. Both experimental and SOLPS-ITER modeling studies of Ne-seeded plasma will be described in this paper. The results of the Ne seeding experiment will be discussed in Section 2. To better understand the process and physics of Ne seeding scenarios, the experimental results will be matched and discussed with SOLPS-ITER simulations in Section 3. Summaries will be provided in the final section.

2. Experiments

a. Fueling system and diagnostics

EAST is uniquely designed to achieve different configurations and directions of magnetic fields. The discharge discussed in this paper was set with the upper single null (USN) divertor configuration. Figure 1 shows that the controlled pulsed Ne impurity was injected through the inlet of the divertor gas puff system and the outer mid-plane (OMP) SMBI system. And inlets on the divertor targets are located near the strike points to cool down the high heat flux in their vicinity[13]. The width and value of puffing pulse can be preset by the Plasma Control System (PCS) before starting a discharge. The SMBI is used for the radiation feedback control. In combination with real-time AXUV measurements, we could achieve different radiation proportions by the feedback control system[16].

Experiment relevant diagnostics are also shown in Figure 1. Upstream electron density and temperature, which are important to SOLPS validation, are measured by Reflectometer and Thomson Scattering (TS). Divertor Langmuir probes can provide downstream plasma characteristics like electron temperature, density and heat flux on divertor targets. The radiated power in the bulk plasma can be obtained by four 16-channels Absolute Extreme Ultraviolet (AXUV) detector arrays. Impurities in the divertor region can be detected by divertor spectroscopy. Details of these diagnostics can be found in Ref[17-21].

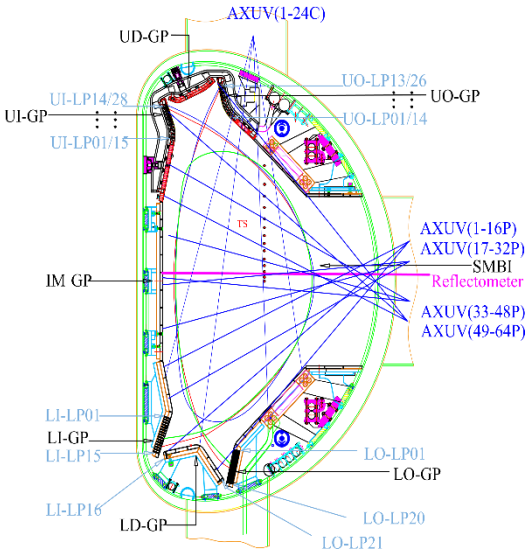

Figure 1. Poloidal cross section of EAST gas puff locations and relevant diagnostics. AXUV: absolute extreme ultraviolet bolometer arrays; SMBI: supersonic molecular beam injection; UI/LI: upper/lower inner target; UO/LO: upper/lower outer target; UD/LD: upper/lower dome; IM: inner midplane; GP: gas puff inlet; LP: Langmuir Probes; TS: Thomson scattering.

b. Parameters and impurity evolution

Shot#71021 is a typical H-mode plasma with USN divertor configuration. The time traces of the main parameters are shown in Figure 2. The plasma current I_p was 450kA and toroidal field B_t was 2.3T. The line averaged density n_e was set to 3×10^{19} m^{-3}. The $B\times\nabla B$ direction pointed toward the upper divertor. The total heating power P_{in} was 3.4MW, including 1.5MW Low Hybrid Waves (LHW) heating and 1.9MW

Neutral Beam Injection (NBI). To reduce the heat load on the divertor target, the Ne/D_2 mixture (Ne:D_2=1:4) was seeded from the UO inlet from t=3s with a pulse for 100 ms. From 4s to 7.5s, the SMBI-Ne pulses (pure Ne) were used for the radiation feedback control, and details of the feedback control regime are provided in Ref[22].

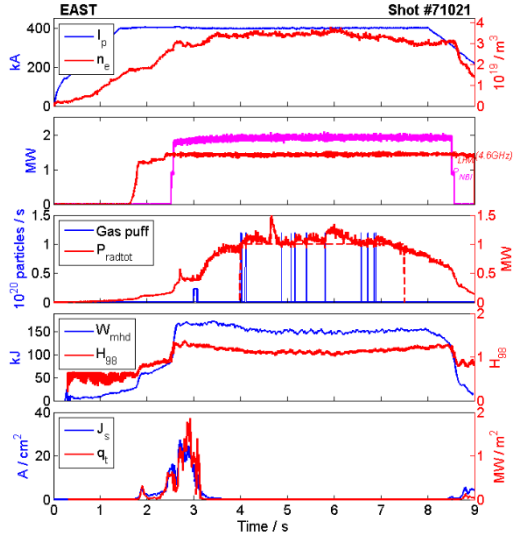

Figure 2. Time evolution of Shot #71021. (a) Line-averaged electron density (n_e) and plasma current (I_p); (b) Auxiliary Heating: 4.6 GHz LHW and NBI; (c) Ne seeding rate and total radiation power; (d) Stored energy(W_{mhd}) and H_{98} factor; (e) Ion and heat flux near the outer strike point.

The target value of total radiation loss (P_{radtot}) in the bulk plasma was set as 1MW (f_{rad}=P_{radtol}/P_{in}~30%). With Ne injection from the divertor, after ~100 ms delay, radiation increased rapidly. P_{radtot} increased from 0.4MW to 1.0MW. In the meantime, averaged density n_e increased to 3.3×10^{19} m^{-3}. Particle and heat fluxes on divertor targets dropped significantly with the radiation increase. Although there was a clear rise of radiation, the stored energy, W_{mhd}, and H_{98} factor dropped only by 6% and 5% respectively. In other words, the plasma confinement remained stable. From 4.0s, the radiation feedback control was performed. When P_{radtot} reached the target value, 1.0MW, and the f_{rad} reached to ~30%, the stored energy decreased by 10kJ and the H_{98} factor dropped to ~1.10. The reason is that the SMBI is located at the outer midplane, and the supersonic pulses with high speed easily enter the core plasma which leads to the losses of confinement. When radiation feedback was switched off, the H_{98} gradually recovered to the state before Ne seeding. It is remarkable that because of the low pumping efficiency in the upper divertor region[23], the total radiation loss reduced slowly but still remained at a high level until 8.5 s.

Figure 3 shows the time evolution of spectrum intensity of the main impurities observed by divertor spectroscopy. Oscillations of the signals resulted from the plasma shape oscillation due to the presence of ELMs. Compared with the Ar-seeded case, there was no obvious W sputtering increase during Ne seeding. Other common impurities in EAST, such as Li and C, were slightly reduced with the increase of Ne. The reason is that Ne is a lower Z impurity compared with Ar. A good Li-coating wall environment could also contribute to the relatively low impurity yield.

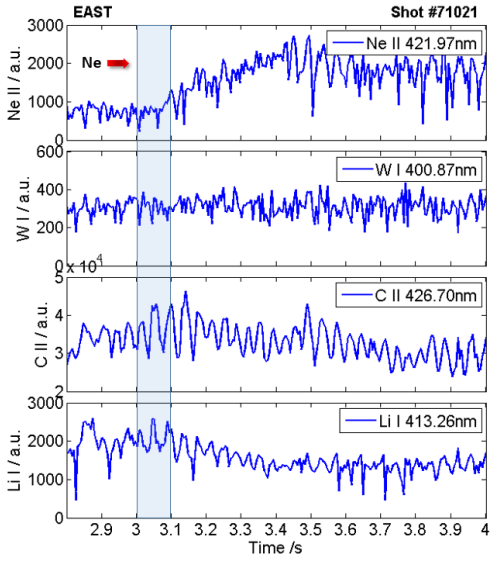

Figure 3. Time trace of the major impurities by the divertor spectroscopy. There is no clear increase of other impurities in the upper divertor region during Ne seeding. Oscillations of the signals resulted from the plasma shape oscillation due to the presence of ELMs

c. Divertor detachment

After the Ne injection, the main parameters in the divertor region changed clearly despite the whole plasma confinement decreased slightly.

In Figure 4, the three time slices of LP measurement are compared: 2.95s (without Ne), 3.15s (onset of detachment), 3.75s (detachment). Before Ne seeding, there was a clear asymmetry between the inner and outer target. The saturation ion current j_s, electron density n_e, electron temperature T_e and heat flux q_t on the outer target were much higher than on the inner target. The peak heat flux was around 1.4MWm^{-2} near the outer strike point (OSP), while it was around 0.2MWm^{-2} on the inner target. After a 100-ms delay, from 3.1s, Ne started to affect the plasma. The shape of the whole plasma slightly changed from 3.1s to 3.4s resulting from the radiation cooling which caused a 3cm shift of the strike point on the UO and a 0.5cm shift on the UI. Similar to the detachment analysis in ASDEX Upgrade, the first state of detachment we defined was detachment onset (3.15s)[24]. From 3.10s, plasma on the UI began to detach. Ignoring the measurement errors, particle and power flux almost disappeared on the UI. There was only a relatively high temperature area in the far SOL region ($\triangle$S$\approx$3-10cm). Top n_e and T_e in this region was 4.0 × 10^{18}m^{-3}, and 29eV respectively. Different from the inner target, UO was still attached to the plasma. Peak ion and heat flux on the UO reduced by 40~50%, but in the far SOL region, j_s and n_e on the UO surprisingly increased slightly instead of decreasing. Different behaviors between UO and UI resulted from the injection position of Ne and asymmetry of the two targets. Also $E \times B$ drifts, which point to the inner target within SOL, also promoted plasma detachment on the inner target. Despite j_s near the OSP decreasing from 23 to 12 Acm^{-2}, and T_e dropping to 34eV, n_e still remained at the initial level.

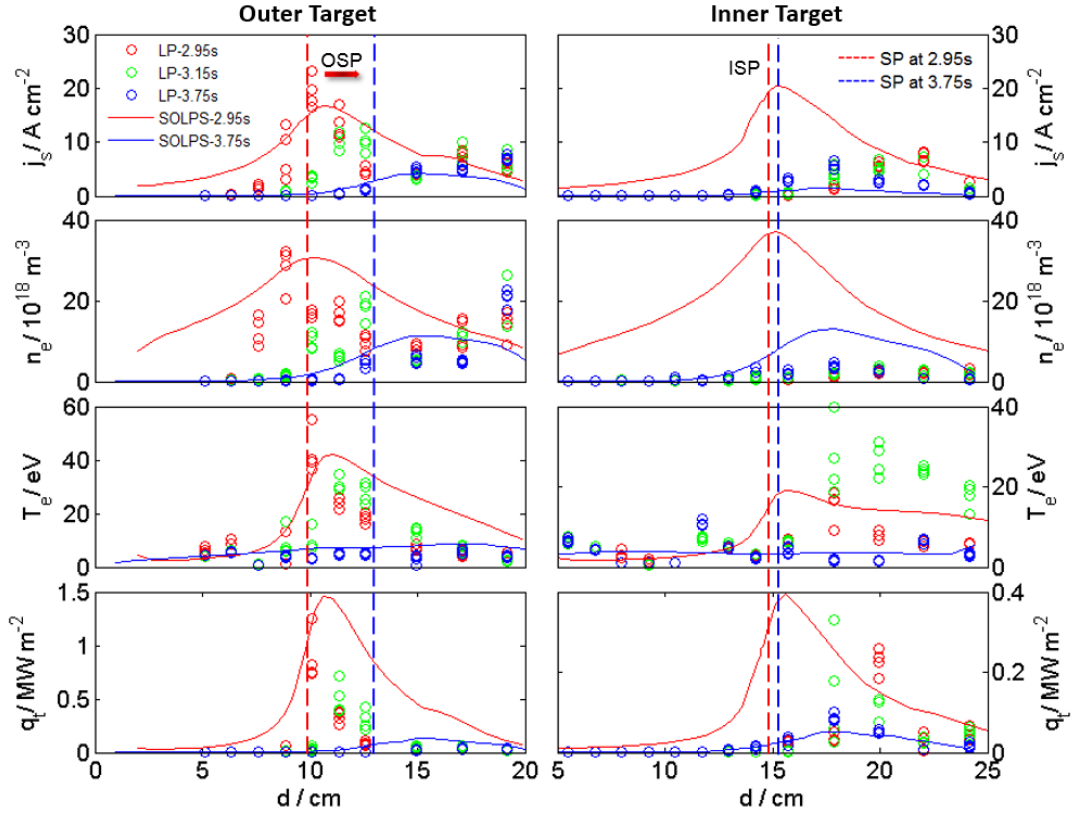

Figure 4. Divertor Profiles from LP measurement (dots) and SOLPS-ITER modeling (lines). Three time slices in the experiment are compared: 2.95s (red), 3.15s (green) and 3.75s (blue). X-axis d represents the distance to divertor corner. The vertical dash lines show locations of the strike points, which moved away from the divertor corner from 2.95s to 3.75s. OSP: Outer Strike Point; ISP: Inner Strike Point.

It is noticed that the OSP shifted to the d=12cm position at this moment. From 3.28s, the UO target also entered the detachment regime. Near the OSP, j_s, n_e as well as T_e reduced sharply to 4Acm^{-2}, 5×10^{18}m^{-3} and 5eV respectively. The ion flux j_s and n_e in the far SOL region only dropped slightly compared with those in the scenario without Ne seeding. The plasma near the strike points detached, but the plasma did not reach the detachment threshold. Therefore, this state was not a completely detached state. Instead it would be more appropriate to call this state as partial detachment referring to the ASDEX Upgrade's experience[4].

This state stopped at 3.77s and lasted only about 0.5s before the SMBI started working because the Ne pulse was only set for 0.1s. There was a clear reduction of q_t on both targets due to the increase of radiation. The heat flux at the OSP was reduced from ~1.5MWm^{-2} to less than 0.1MWm^{-2}. This shows that Ne has a relatively high efficiency in reducing heat flux on the divertor target. Asymmetry between the two targets was also significantly suppressed. Radiation distribution during this period will be compared with simulations and discussed in the next section.

3. SOLPS-ITER modelling

To understand the physics behind the radiative divertor experiment, the code package SOLPS (Scrape Off Layer Plasma Simulator) was introduced for numerical simulations. The simulation results in this paper were calculated by the new package of SOLPS code, SOLPS-ITER, which is mainly developed and maintained by ITER Organization. The SOLPS-ITER aims at the ITER divertor design and edge plasma physics in future devices. Similar to the previous versions, SOLPS-ITER consists of two main coupled codes, a fluid model solver B2.5 and a neutral transport solver Eirene, as well as a series of tools for generating meshes and input files, analyzing and postprocessing[25, 26]. Two time slices were picked for the simulation in the discharge Shot #71021, 2.95s (without Ne seeding) and 3.75s (with Ne seeding), for discussion.

a. Mesh and input

The mesh was generated by modules incorporated into SOLPS-ITER, as shown in Figure 5, which includes a field-aligned quadrilateral mesh for B2.5 and a triangular mesh for Eirene.

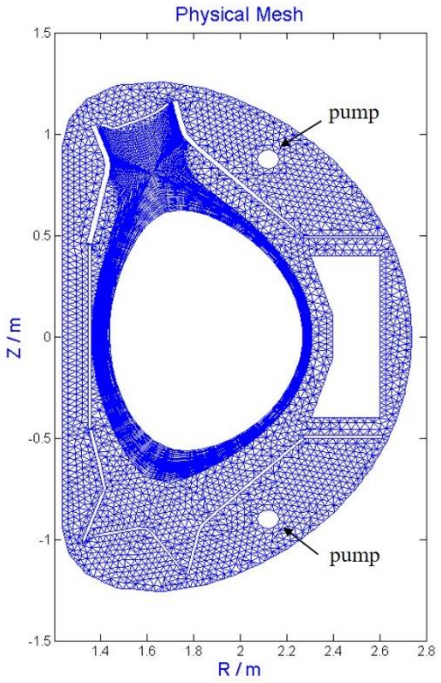

Figure 5. Physical mesh for Shot #71021(2.95s) in SOLPS-ITER. The mesh consists of a field-aligned quadrilateral mesh inside for B2.5 and a triangular mesh for Eirene.

The geometrical structure consists of the tungsten divertor (top), the carbon divertor (bottom), upper and lower cryopumps, other PFCs and the vacuum chamber. The equilibrium was provided by the equilibrium fitting (EFIT) code. It is worth noting the grids use two different equilibriums because the plasma shape at 2.95s and 3.75s changed slightly. By balancing the simulation time cost and accuracy, the mesh for fluid is 96×36 (poloidal×radial). The computational region of this USN plasma can be divided into three parts:

the "core" region (between the core boundary and separatrix), the SOL region and the private flux region (PFR). The width of this grid was around 4cm at the outer midplane. The gas puff inlet is marked in Figure 1.

In these simulations, the fluid model only included D and Ne species. The sputtered W species were ignored because there was no obvious W sputtering increasing in the experiment. Therefore, we can assume the background W as a core radiation source but not the W species in the fluid because they mainly ionize in the plasma core region outside of the SOLPS mesh.

Considering the absorbing efficiency of auxiliary heating[27, 28], the input power for the case without and with Ne seeding was 2.3MW and 2.0MW(assumed the radiation in the inner core, inside the mesh, 0.3MW), respectively. The electron density, n_e, at the separatrix was set to 1.29×10^{19}m^{-3} with feedback fueling at the midplane. The decay length for the temperature at the SOL boundary was set to 1cm. Constant poloidal transport coefficients were used in both cases. The perpendicular transport coefficients were set according to the previous experience[14, 29, 30]. The simulated upstream profile of using different sets of these coefficients have to be matched with experiment measurement at OMP. Details will be discussed in Section 3.b.

Neutral Ne was seeded at the rate of 1.9×10^{19} particles/s from the gas puff inlet in the case with Ne seeding. The pumping surfaces have been indicated in Figure 5. The total pumping rate was around 60m^3/s at 298K, which is estimated from the cryo-pump pumping rate minus the seeding rate from the NBI. The D and Ne ions were set to be fully recycled. In addition, considering the size of the machine and the mesh, we assumed all the neutrals 'pumped' by the core boundary would return to the simulating region as fully ionized ions (D^+ and Ne^{10+}). Drifts were ignored in these cases due to the instability when simulating impurity species.

b. Results and discussion

The experimental upstream T_e and n_e at t=2.95s and 3.75s are shown in Figure 6(a). In SOLPS simulation it is important to match the density and temperature profiles well first in the upstream plasma because the divertor conditions (downstream) are sensitive to upstream parameters[31]. These coefficients were continually modified for matching temperature and density profiles, especially the upstream profile, until we obtained a suitable set of coefficients (Figure 6(b)) that made the upstream profile consistent with the experimental results.

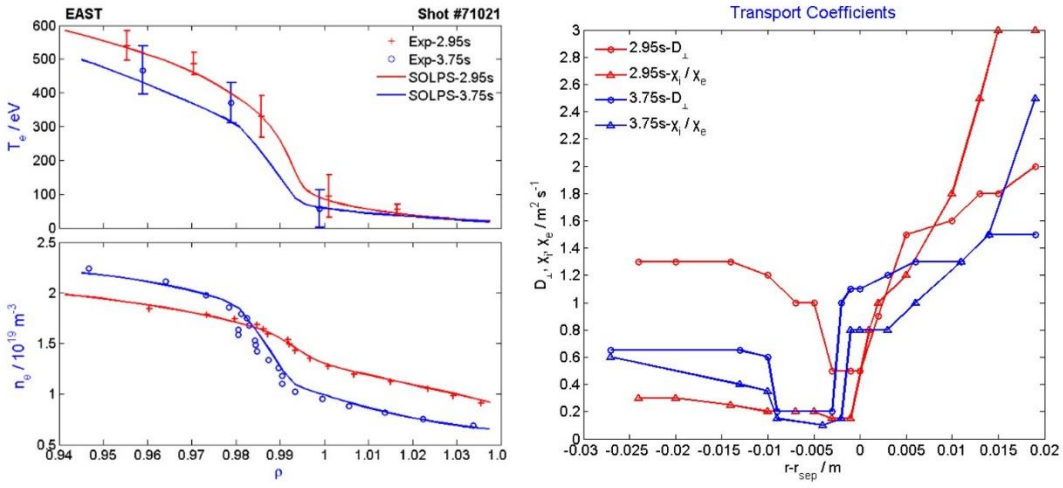

Figure 6. (a) Experimental (dots) and simulated(lines) profiles of upstream T_e, n_e. (b) Profiles of the radial transport coefficients at the OMP for t=2.95s and t=3.75s respectively.

Pinch velocities were ignored. Diffusion coefficients were set to the same value for all charged species. Variation of many parameters such as collisionality, density/thermo gradients, and turbulence due to Ne seeding could change the transport characteristic[1]. This is also the reason for using different transport coefficients in the two cases.

Both simulated electron density and temperature match well with the experimental measurements (Figure 6(a)). The electron density was provided by reflectometer, while the electron temperature was provided by Thomson Scattering. There was a clear edge transport barrier (ETB) near the LCFS (Last Closed Flux Surface). After the Ne seeding, T_e reduced by 30eV at the LCFS and by 70eV at the $\rho = 0.95$ position. The barrier of T_e at 3.75s shifted inside the LCFS by ~2mm, and was flatter than at 2.95s. Contrary to the T_e, the n_e barrier became steeper at 3.75s, and it shifted by ~3mm inside the LCFS. There was a clear decline of n_e from $1.29 \times 10^{19} m^{-3}$ to $0.99 \times 10^{19} m^{-3}$ at LCFS, but near the core boundary, $\rho = 0.95$, n_e increased to 2.1×10^{19} m^{-3} . It can be seen that Ne seeding clearly influenced the upstream T_e and n_e profile. Apart from the reduction of temperature, the n_e gradient also changed inside the LCFS with Ne seeding. It is deduced that the plasma shape shrank due to radiation cooling.

In the divertor region the transport coefficients were taken to be constant with $D_\perp = 3.0 m^2/s$, $\chi_i = \chi_e = 2.5$ m^2/s in the case without Ne seeding, and $D_\perp = 1.0 m^2/s$, $\chi_i = \chi_e = 8.0 m^2/s$ in the case with Ne seeding respectively. Different from the upstream match, the profiles on the targets do not agree so well with the diagnostics. Figure 4 shows the simulated profiles of j_s, n_e, T_e, and q_t on two targets. In the absence of drifts, it might be difficult to make good agreements on both targets. Therefore, we prefer matching well on the outer target, which has higher particle and heat fluxes to make comparisons of seeded and unseeded scenarios. At 2.95s, the well-matched results were only achieved on the outer target. The peak value of T_e and q_t matched well with diagnostics, while j_s was slightly lower and n_e was higher than the measurements. The simulated profile had a similar trend to the diagnostics, but the half-peak width of the simulation results was wider than in the experiment. The reason could be that a constant transport coefficient was used in the divertor region. It is worth noting that the position of the peak in simulation shifts 1-2 cm from the peak of LP data because of the absence of drifts. Also, due to ignoring the drifts, there is large gap between the modeling and experimental results on the inner target. The modelled flux, density and temperature were much higher than the LP measurement. In particular, when the T_e was quite high at 2.95s, the effect of ignoring drifts was clearer than the plasma with lower electron temperature[32, 33].

At 3.75s, the situation was much better than the case of t=2.95s. Profiles of j_s, n_e, T_e and q_t were in good agreement with the diagnostics except for the far SOL region on UO. The reason is that the plasma on the UO is in a partial detachment regime and there were still fluxes in far SOL region while SOLPS-ITER is difficult to match this situation due to the absence of drifts. On the UI, simulated n_e and T_e were slightly higher than in the experimental results. The asymmetry between the two targets was significantly reduced due to the clear decrease of flux on the UO.

Radiation distribution is also one of our concerns. At 3.75s, total radiation power in SOLPS modeling increased to 1.2MW. Considering there was 0.3 MW core radiation in our initial assumption, the total radiation loss was 1.5 MW, and the radiation fraction f_{rad} was around 45%, which was higher than measurement in Ref[22]. This is because in this simulation work, the calculated radiation include line radiation, bremsstrahlung and

power loss due to atom radiation in the vacuum, while in the experiment, the radiation was only measured in the main plasma by AXUV. The ratio of radiation caused by various speicies to total radiation losses was also analyzed, and radiation caused by Ne^{4+} to Ne^{7+} occupied a dominant proportion (around 75%).

However, in our experience and from former investigations in JT-60U[34], the proportion of radiation induced by Ne impurity was not as high as in the simulation. Not only the Ne but other low-Z impurities, such as Li and C, also play important roles in particle and power dissipation. The amount of these impurities will increase due to the physical sputtering in the presence of Ne impurity. Accurate counts and sputtering factors have to be verified by further experiments.

Due to the limitations in the scope of observation of vertical AXUV arrays, as Figure 1 shows, tomographic reconstruction of a 2D radiation profile is difficult to achieve in the upper divertor region. However, 2D radiation distribution is easily obtained in SOLPS simulation, assuming that we could achieve good agreements with the radiation profile in 1D horizontal AXUV measurements. Therefore, the 2D radiation distribution given in this case would be a reasonable solution for discussion.

Figure 7 shows horizontal AXUV arrays distribution and the comparison between the experimental and modeling results. The modelled profiles are basically consistent with the measurements. The peak value appeared at the Z=0.65 m position denoting the observation line through the X-point, but the peak in experiment moved to the Z=0.69 m position, which means that the real main radiation zone was more concentrated in the divertor region than in the simulation. Figure 8 shows the 2D profile of radiation loss in the Ne seeding case. In the vicinity of the X-point, radiation losses increased significantly at low T_e; a typical MARFE (Multifaceted Asymmetric Radiation From the Edge) appeared. Similar results were also observed in impurity seeding experiments in JET[35] and JT-60U[36].

According to the collisional-radiative model, the radiation loss, namely the sum of line radiation, recombination-induced radiation and bremsstrahlung, can be estimated by $P_{rad} \approx L_z(T_e)n_z n_e$, where L_z is the cooling factor of impurities depending on the impurity atoms and electron temperatures[37]. From the ADAS database, the peak intervals of L_z(Ar) are located around T_e=10-30eV and T_e=150-250eV respectively, which correspond to the T_e in the divertor region and the pedestal region. The

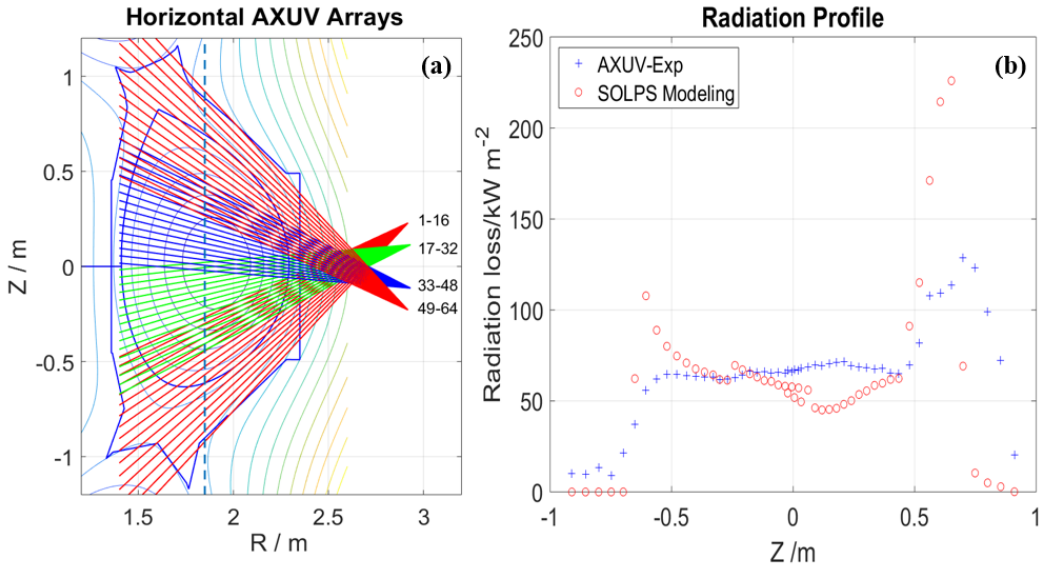

Figure 7. (a) Horizontal AXUV Arrays (b) 1D Radiation losses distribution of the experimental and modeling results.

peak L_z of N appears at the T_e of around 15eV, which also corresponds to the divertor region T_e. While there is a peak for the L_z(Ne) between 20-40eV, which is at the same level of T_e near the X-point. That is why behavior of Ne is different from that of Ar and N_2. The vicinity of the X-point locates around closed field-lines and neutral densities are rather small. The relatively low temperature caused by the radiation will lead to quite high densities in this region due to the pressure constancy along field-lines. With n_e rising, P_{rad} will increase further. Considering quite high radiation and the weak parallel heat conduction when T_e is relatively low in this region, a thermal collapse will occur. Therefore, the reasons above promote the formation of a MARFE in this region[38, 39].

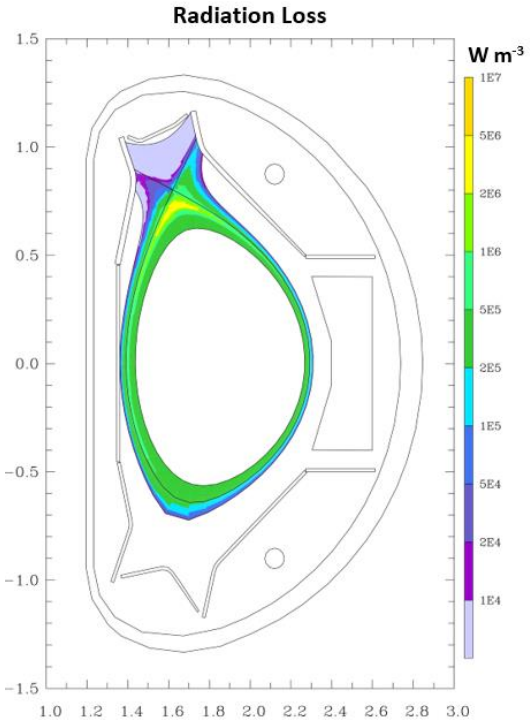

Figure 8. Radiation losses profile by SOLPS simulation. There is a clear MARFE in the vicinity of the X-point, which is consistent with experiment observation.

Through energy balance analysis, we found that a large proportion (70%) of the radiation came from the core region. The total radiation emanating for the MARFE region itself is estimated to be around 0.45MW. Apart from the radiation in the core region, there was only 0.4MW radiation in total in the SOL and PFR region. The power across the separatrix is around 1.3MW. A part of it was dissipated by radiation, and the rest of the energy was deposited onto the targets. Integrating the power flux on the both targets, the total power on outer target and inner target was 0.09MW and 0.06 MW respectively, while the power was 0.8MW and 0.4MW before Ne injection. The combination of the experimental and simulation results suggest that the power load on the targets was effectively controlled regardless of the distribution of the radiation.

The fuel dilution has also to be considered. Ne exhibited relatively high dilution in the core plasma. Z_{eff} at LCFS on OMP was up to 7.9. Divertor compression is the ratio of the averaged impurity density in the divertor region to the core ($c_{Ne}=n_{Ne,div}/n_{Ne,core}$). It reveals how much Ne is confined in the divertor region, which is also an important factor in evaluating screening effects in impurity seeding experiments. In this case, the ratio at 3.75s was 1.5, while it was 1.8 in previous Ar seeding experiments[29]. This shows that Ne compared with Ar more easily leads to more core-localized radiation, which is consistent with the radiation distribution in the experiment and the simulation. For ITER and future devices, the high dilution and radiation in the core plasma region would risk reducing the rate of fusion reaction. However, there are also some opinions thinking that[35] in future devices the pedestal impurity transport might be different from current devices due to the higher pedestal temperature gradients and lower density gradients. The screening performance would be better in this environment. Ne might be still possible to be an option of the radiator for power exhaust. Nevertheless, it is an urgent need to find a way to avoid excessive contamination in the core plasma region in future devices.

4. Summary

Both experimental and numerical investigation of Ne radiative divertor plasma were carried out in EAST. With the simultaneous Ne seeding from the divertor gas puff inlet and midplane SMBI, radiation feedback H-mode plasmas were achieved. The high efficiency of Ne in plasma cooling was proved and there was only a slight reduction of plasma confinement during Ne seeding. For ITER and future devices, Ne seeding is as efficient as Ar seeding to meet the requirement to produce detachment for avoidance of overheating on divertor targets. Characteristics of partial detachment caused by Ne seeding were also discussed. Both density and temperature started to decrease in the detachment onset state but there was a relatively high T_e zone in the far SOL region on the UI target. Plasma partially detached at 3.75s. Despite the density in the far SOL region remaining stable on the UO target, electron temperature, heat flux and in-out asymmetry reduced rapidly. Furthermore, there was no obvious wall sputtering during the Ne seeding. The Ne-seeded radiative divertor experiment was also validated by SOLPS-ITER code on EAST. The simulation results basically agreed well with the experiment. This shows that Ne has a relatively good performance in reducing particle fluxes and heat load on targets. But it is difficult to match parameters well on both targets when ignoring drifts. Through reconstruction of radiation distribution by SOLPS Code, most of the radiation caused by Ne impurity distributed in the region inside the separatrix. There was a clear MARFE region in the vicinity of the X-point.

Higher fuel dilution and lower divertor compression in the Ne seeding scenario than in the Ar seeding scenario. Although power load on the divertor targets can be dissipated effectively in Ne radiative regime, the high dilution and radiation in the core plasma region would risk reducing the rate of fusion reaction in ITER and future devices. This is important to consider if Ne is used as the radiator in the future.

Acknowledgement

This work was partially supported by National MCF Energy R&D Program of China under contract number of 2018YFE0303103, the National Natural Science Foundation of China No.11875287, No.11575242 and No.11705233 Projects, Chinses Scholarship Council with No.201706340013 Program and Key Research Program of Frontier Sciences, CAS, Grant NO. QYZDB-SSW-SLH001. Many thanks to M. Wischmeier, O. Pan, M.L. Zhao, L.Y. Xiang, H.S. Wu and other colleagues from IPP-Garching for their contributions and comments to this paper.

References

1. A. Loarte, B. Lipschultz, A. S. Kukushkin, G. F. Matthews, P. C. Stangeby, N. Asakura, G. F. Counsell, G. Federici, A. Kallenbach, K. Krieger, A. Mahdavi, V. Philipps, D. Reiter, J. Roth, J. Strachan, D. Whyte, R. Doerner, T. Eich, W. Fundamenski, A. Herrmann, M. Fenstermacher, P. Ghendrih, M. Groth, A. Kirschner, S. Konoshima, B. LaBombard, P. Lang, A. W. Leonard, P. Monier-Garbet, R. Neu, H. Pacher, B. Pegourie, R. A. Pitts, S. Takamura, J. Terry, E. Tsitrone and I. S.-o. L. D. Phy, Nuclear Fusion **47** (6), S203-S263 (2007).

2. F. Reimold, M. Wischmeier, M. Bernert, S. Potzel, A. Kallenbach, H. W. Müller, B. Sieglin and U. Stroth, Nuclear Fusion **55** (3), 033004 (2015).

3. F. Reimold, M. Wischmeier, M. Bernert, S. Potzel, D. Coster, X. Bonnin, D. Reiter, G. Meisl, A. Kallenbach, L. Aho-Mantila, U. Stroth and A. U. Team, Journal of Nuclear Materials **463**, 128-134 (2015).

4. A. Kallenbach, M. Bernert, M. Beurskens, L. Casali, M. Dunne, T. Eich, L. Giannone, A. Herrmann, M. Maraschek, S. Potzel, F. Reimold, V. Rohde, J. Schweinzer, E. Viezzer and M. Wischmeier, Nuclear Fusion **55** (5), 053026 (2015).

5. L. Y. Xiang, M. Wischmeier, D. Coster, M. Bernert, H. Y. Guo and G. N. Luo, Nuclear Materials and Energy **12**, 1146-1151 (2017).

6. A. W. Leonard, Fusion Science and Technology **48** (2), 1083-1095 (2005).

7. G. P. Maddison, C. Giroud, B. Alper, G. Arnoux, I. Balboa, M. N. A. Beurskens, A. Boboc, S. Brezinsek, M. Brix, M. Clever, R. Coelho, J. W. Coenen, I. Coffey, P. Belo, S. Devaux, P. Devynck, T. Eich, R. C. Felton, J. Flanagan, L. Frassinetti, L. Garzotti, M. Groth, S. Jachmich, A. Jarvinen, E. Joffrin, M. A. H. Kempenaars, U. Kruezi, K. D. Lawson, M. Lehnen, M. J. Leyland, Y. Liu, P. J. Lomas, C. G. Lowry, S. Marsen, G. F. Matthews, G. K. McCormick, A. G. Meigs, A. W. Morris, R. Neu, I. M. Nunes, M. Oberkofler, F. G. Rimini, S. Saarelma, B. Sieglin, A. C. C. Sips, A. Sirinelli, M. F. Stamp, G. J. van Rooij, D. J. Ward, M. Wischmeier and J. E. Contributors, Nuclear Fusion **54** (7), 073016 (2014).

8. N. Asakura, T. Nakano, N. Oyama, T. Sakamoto, G. Matsunaga and K. Itami, Nuclear Fusion **49** (11), 8 (2009).

9. M. L. Reinke, J. W. Hughes, A. Loarte, D. Brunner, I. H. Hutchinson, B. LaBombard, J. Payne and J. L. Terry, Journal of Nuclear Materials **415** (1), S340-S344 (2011).

10. B. N. Wan, J. G. Li, H. Y. Guo, Y. F. Liang, G. S. Xu, L. Wang, X. Z. Gong, A. Garofalo and E. T. Collaborators, Nuclear Fusion **55** (10), 20 (2015).

11. D. M. Yao, G. N. Luo, Z. B. Zhou, L. Cao, Q. Li, W. J. Wang, L. Li, S. G. Qin, Y. L. Shi, G. H. Liu and J. G. Li, Physica Scripta **2016** (T167), 014003 (2016).

12. H. Y. Guo, J. Li, X. Z. Gong, B. N. Wan, J. S. Hu, L. Wang, H. Q. Wang, J. E. Menard, M. A. Jaworski, K. F. Gan, S. C. Liu, G. S. Xu, S. Y. Ding, L. Q. Hu, Y. F. Liang, J. B. Liu, G. N. Luo, H. Si, D. S. Wang, Z. W. Wu, L. Y. Xiang, B. J. Xiao, L. Zhang, X. L. Zou, D. L. Hillis, A. Loarte, R. Maingi and E. Team, Nuclear Fusion **54** (1) (2014).

13. J. Chen, Y. Duan, Z. Yang, L. Wang, K. Wu, K. Li, F. Ding, H. Mao, J. Xu, W. Gao, L. Zhang, J. Wu, G.-N. Luo and E. Team, Chinese Physics B **26** (9) (2017).

14. Z. S. Yang, J. B. Chen, D. P. Coster, Y. M. Duan, L. Wang, F. Ding, J. C. Xu, Q. Zang, T. F. Wang, N. Yan, T. Zhang, L. Zhang, J. H. Wu, Y. K. M. Peng and G. N. Luo, Phys. Plasmas **24** (1), 8 (2017).

15. A. Kallenbach, M. Bernert, R. Dux, L. Casali, T. Eich, L. Giannone, A. Herrmann, R. McDermott, A. Mlynek, H. W. Müller, F. Reimold, J. Schweinzer, M. Sertoli, G. Tardini, W. Treutterer, E. Viezzer, R. Wenninger and M. Wischmeier, Plasma Physics and Controlled Fusion **55** (12), 124041 (2013).

16. K. Wu, Q. P. Yuan, B. J. Xiao, J. B. Chen, Y. M. Duan, X. W. Zheng, L. Wang, Z. P. Luo and X. J. Liu, Fusion Engineering and Design **129**, 291-293 (2018).

17. Y. M. Wang, X. Gao, B. L. Ling, S. B. Zhang, T. Zhang, X. Han, S. C. Liu, Z. X. Liu, Y. Liu, A. Ti and E. Team, Fusion Engineering and Design **88** (11), 2950-2955 (2013).

18. Q. Zang, J. Y. Zhao, L. Yang, Q. S. Hu, Y. Q. Jia, T. Zhang, X. Q. Xi, S. H. Bhatti and X. Gao, Plasma Science & Technology **12** (2), 144-148 (2010).

19. J. C. Xu, L. Wang, G. S. Xu, G. N. Luo, D. M. Yao, Q. Li, L. Cao, L. Chen, W. Zhang, S. C. Liu, H. Q. Wang, M. N. Jia, W. Feng, G. Z. Deng, L. Q. Hu, B. N. Wan, J. Li, Y. W. Sun and H. Y. Guo, Review of Scientific Instruments **87** (8), 083504 (2016).

20. Y. M. Duan, L. Q. Hu, S. T. Mao, P. Xu, K. Y. Chen, S. Y. Lin, G. Q. Zhong, J. Z. Zhang, L. Zhang and L. Wang, Plasma Science & Technology **13** (5), 546-549 (2011).

21. H. Mao, F. Ding, G.-N. Luo, Z. Hu, X. Chen, F. Xu, Y. Zhongshi, C. Jingbo, W. Liang, R. Ding, Z. Ling, G. Wei, J. Xu and C. Wu, Review of Scientific Instruments **88** (4), 043502 (2017).

22. K. Wu, Q. P. Yuan, B. J. Xiao, L. Wang, Y. M. Duan, J. B. Chen, X. W. Zheng, X. J. Liu, B. Zhang, J. C. Xu, Z. P. Luo, Q. Zang, Y. Y. Li, W. Feng, J. H. Wu, Z. S. Yang, L. Zhang, G. N. Luo, X. Z. Gong, L. Q. Hu, J. S. Hu and J. Li, Nuclear Fusion **58** (5) (2018).

23. H. Liu, L. Wang, G. S. Xu, F. Ding, J. B. Liu, J. C. Xu, W. Feng, G. Z. Deng, X. W. Zheng, Y. W. Yu, H. Si, H. Q. Liu, Q. Q. Yang, Z. Sun and H. Y. Guo, Plasma Science & Technology **19** (9), 7 (2017).

24. S. Potzel, M. Wischmeier, M. Bernert, R. Dux, H. W. Muller, A. Scarabosio and A. U. Team, Nuclear Fusion **54** (1), 19 (2014).

25. X. Bonnin, W. Dekeyser, R. Pitts, D. Coster, S. Voskoboynikov and S. Wiesen, Plasma and Fusion Research **11**, 1403102-1403102 (2016).

26. S. Wiesen, D. Reiter, V. Kotov, M. Baelmans, W. Dekeyser, A. S. Kukushkin, S. W. Lisgo, R. A. Pitts, V. Rozhansky, G. Saibene, I. Veselova and S. Voskoboynikov, Journal of Nuclear Materials **463**, 480-484 (2015).

27. F. K. Liu, B. J. Ding, J. G. Li, B. N. Wan, J. F. Shan, M. Wang, L. Liu, L. M. Zhao, M. H. Li, Y. C. Li, Y. Yang, Z. G.

Wu, J. Q. Feng, H. C. Hu, H. Jia, Y. Y. Huang, W. Wei, M. Cheng, L. Xu, Q. Zang, B. Lyu, S. Y. Lin, Y. M. Duan, J. H. Wu, Y. Peysson, J. Decker, J. Hillairet, A. Ekedahl, Z. P. Luo, J. P. Qian, B. Shen, X. Z. Gong, L. Q. Hu and E. Team, Nuclear Fusion **55** (12), 11 (2015).

28. C. D. Hu, Y. H. Xie, Y. L. Xie, S. Liu, Y. J. Xu, L. Z. Liang, C. C. Jiang, P. Sheng, Y. M. Gu, J. Li and Z. M. Liu, Plasma Science & Technology **17** (10), 817-825 (2015).

29. L. Y. Xiang, H. Y. Guo, M. Wischmeier, Z. W. Wu, L. Wang, Y. M. Duan, K. F. Gan, Y. C. Shen, Y. Chen and E. Team, Phys. Plasmas **24** (9), 10 (2017).

30. X. J. Liu, G. Z. Deng, L. Wang, S. C. Liu, L. Zhang, G. Q. Li and X. Gao, Phys. Plasmas **24** (12), 7 (2017).

31. W. Dekeyser, X. Bonnin, S. W. Lisgo, R. A. Pitts, D. Brunner, B. Labombard and J. L. Terry, Plasma and Fusion Research **11**, 1403103-1403103 (2016).

32. P. C. Stangeby and A. V. Chankin, Nuclear Fusion **36** (7), 839-852 (1996).

33. V. Rozhansky, E. Kaveeva, S. Voskoboynikov, A. H. Bekheit, D. Coster, X. Bonnin and R. Schneider, Journal of Nuclear Materials **313-316**, 1141-1149 (2003).

34. T. Nakano and J. T. Team, Journal of Nuclear Materials **463**, 555-560 (2015).

35. M. Bernert, M. Wischmeier, A. Huber, F. Reimold, B. Lipschultz, C. Lowry, S. Brezinsek, R. Dux, T. Eich, A. Kallenbach, A. Lebschy, C. Maggi, R. McDermott, T. Putterich and S. Wiesen, Nuclear Materials and Energy **12**, 111-118 (2017).

36. H. Kubo, S. Sakurai, S. Higashijima, H. Takenaga, K. Itami, S. Konoshima, T. Nakona, Y. Koide, N. Asakura, K. Shimizu, T. Fujita and K. W. Hill, Journal of Nuclear Materials **313**, 1197-1201 (2003).

37. J. Wesson, *Tokamaks*. (Oxford University Press, Oxford, United Kingdom, 2004).

38. R. Schneider, X. Bonnin, K. Borrass, D. P. Coster, H. Kastelewicz, A. Reiter, V. A. Rozhansky and B. J. Braams, Contributions to Plasma Physics **46** (1-2), 3-191 (2006).

39. P. C. Stangeby, *The Plasma Boundary of Magnetic Fusion Devices*. (Institute of Physics Publishing, Bristol, 2000).